Chemotactic Motility-Induced Phase Separation

Hongbo Zhao, Andrej Košmrlj, and Sujit S. Datta

Phys. Rev. Lett. **131**, 118301 — Published 12 September 2023

DOI: 10.1103/PhysRevLett.131.118301

Chemotactic motility-induced phase separation

Hongbo Zhao,[1] Andrej Košmrlj,[2,3] and Sujit S. Datta[1,*]

[1] *Department of Chemical and Biological Engineering, Princeton University, Princeton, NJ 08544*

[2] *Department of Mechanical and Aerospace Engineering, Princeton University, Princeton, NJ 08544*

[3] *Princeton Materials Institute, Princeton University, Princeton, NJ 08544*

(Dated: August 25, 2023)

Collectives of actively-moving particles can spontaneously separate into dilute and dense phases—a fascinating phenomenon known as motility-induced phase separation (MIPS). MIPS is well-studied for randomly-moving particles with no directional bias. However, many forms of active matter exhibit collective chemotaxis, directed motion along a chemical gradient that the constituent particles can generate themselves. Here, using theory and simulations, we demonstrate that collective chemotaxis strongly competes with MIPS—in some cases, arresting or completely suppressing phase separation, or in other cases, generating fundamentally new dynamic instabilities. We establish principles describing this competition, thereby helping to reveal and clarify the rich physics underlying active matter systems that perform chemotaxis, ranging from cells to robots.

The thermodynamics of active matter—collections of agents that consume energy to move or exert forces—has been studied extensively due to its fundamental richness as well as its importance to diverse applications [1, 2]. One prominent class of active matter is that composed of self-propelled agents, ranging from enzymes [3–5] and cells [6–9] to synthetic microswimmers and robots [10–12]. These forms of active matter can often be modeled as collections of Active Brownian Particles (ABPs), each of which self-propels with a velocity of magnitude U_0 and a direction that is continually reoriented by random thermal fluctuations, eventually decorrelating over a time scale τ_R. The persistence length of an ABP trajectory is then given by $\sim U_0\tau_R$; the directedness of a particle of radius a can therefore be described by the reorientation Péclet number $\mathrm{Pe_R} \equiv a/(U_0\tau_R)$.

Studies of this canonical model have led to fascinating insights into the thermodynamics of active matter. For example, phase separation in passive equilibrium systems typically requires attractive interactions between constituents; in stark contrast, for small $\mathrm{Pe_R}$, ABPs undergo motility-induced phase separation (MIPS) into dense and dilute phases without attractive interactions [13–18]. Surprisingly, this non-equilibrium process can often be described using models inspired by the phase separation of thermally-equilibrated passive systems [15, 19–22].

This prior work focused on ABPs that move randomly, with no preferred direction. However, many forms of active matter exhibit collective *chemotaxis*—directed motion in response to an external chemical gradient that can be generated collectively by the agents themselves. In biology, this phenomenon enables populations of cells to escape from harmful environments, colonize new terrain, and migrate as groups [6, 23–32]; at the subcellular level, enzymes may also perform chemotaxis [3–5]. Synthetic active materials that can perform chemotaxis have also been developed, often exhibiting new surprises in their phase behavior—e.g., unusual clustering and oscillatory density fluctuations [10, 11, 33–42]. However, despite these hints that chemotaxis can influence the physics of active matter, a broader understanding of how exactly chemotaxis alters MIPS remains lacking.

Here, we address this gap in knowledge by developing a theoretical model that combines both MIPS and chemotaxis, which are usually studied in isolation. We find that collective chemotaxis can dramatically suppress MIPS, arrest phase separation, or engender new complex phase separation dynamics reminiscent of other pattern-forming systems [43–59], but that arise due to completely different physics—in this case, due to the competition between MIPS, which drives ABPs to cluster into dense phases, and chemotaxis, which instead drives them to disperse away.

Governing equations. Building on existing continuum models of MIPS [15, 19–22], we describe the time evolution of the volume fraction ϕ of *chemotactic* ABPs via the continuity equation,

$$\frac{\partial\phi}{\partial t} = -\nabla\cdot\mathbf{J}, \tag{1}$$

$$\mathbf{J} = \underbrace{-M_0\phi\nabla\big(\tilde{\mu}_h(\phi,\mathrm{Pe_R}) - \kappa\nabla^2\phi\big)}_{\text{MIPS}} + \underbrace{\chi_0\phi\nabla f(\tilde{c})}_{\text{chemotaxis}}, \tag{2}$$

where t is time and $\mathbf{J}$ is the flux of particles. This flux has two contributions, as indicated by the underbraces in Eq. (2). The first reflects active Brownian motion, as established by the classical "model B"; in future work, it would be interesting to explore other models of MIPS that treat additional complexities [20]. As detailed in §1 of [60], $M_0 = 0.5U_0^2\tau_R$ is the active diffusivity reflecting the random undirected motion of the particles, $\tilde{\mu}_h$ is the bulk chemical potential nondimensionalized by

the energy scale $0.5\zeta U_0^2\tau_R$ with drag coefficient ζ, and the characteristic length scale $\sqrt{\kappa} \sim U_0\tau_R$ sets the width of the interface between the dense and dilute phases in MIPS [15, 19].

The second term in Eq. (2) represents a new addition of chemotaxis to this classical model of MIPS. This term is widely used to describe the chemotaxis of microorganisms [6, 24–32, 77] as well as many synthetic forms of active matter [4, 34, 78, 79]; indeed, it can be directly derived from an explicit microscopic description of chemotactic ABPs as detailed in §2 of [60], based on [34]. Here, $\tilde{c}$ is the concentration, nondimensionalized by a fixed characteristic concentration, of a diffusible chemical signal (the *chemoattractant*) that the particles sense and direct their motion in response to. The monotonically-increasing function $f(\tilde{c})$ describes the ability of the particles to sense the chemoattractant; we take $f(\tilde{c}) = \tilde{c}$ as an illustrative example [80, 81]. The chemotactic coefficient χ_0 describes the ability of the particles to move up the sensed chemoattractant gradient. Thus, $\chi_0\nabla f(\tilde{c})$ describes the chemotactic velocity, and when multiplied by ϕ describes the chemotactic flux [82, 83]. Hence, we define a new chemotactic Péclet number $\mathrm{Pe_C} \equiv \chi_0/M_0$ to describe the competition between directed chemotaxis and undirected active diffusion.

Chemoattractants (e.g., nutrients) are often taken up by the particles themselves—thereby collectively generating a local chemoattractant gradient that the particles bias their motion in response to [24–26, 28, 34, 37, 39, 40, 84–88]. Thus, we describe the chemoattractant via

$$\frac{\partial\tilde{c}}{\partial t} = D_c\nabla^2\tilde{c} - k\phi g(\tilde{c}) + S, \tag{3}$$

where D_c is the chemoattractant diffusivity, k is the characteristic volumetric rate of chemoattractant uptake, and $g(\tilde{c})$ describes how uptake rate increases with $\tilde{c}$; we use the linearized $g(\tilde{c}) = \tilde{c}$ for simplicity. Finally, S represents the rate at which chemoattractant is externally supplied, taken to be constant and spatially uniform as an illustrative example.

Chemotaxis suppresses MIPS. First, we establish the conventional case of MIPS as a baseline, described by our governing Eqs. (1)–(3) with $\mathrm{Pe_C} = 0$. To do so, we choose a functional form for $\tilde{\mu}_h(\phi, \mathrm{Pe_R})$, given by Eq. (S4) of [60], that derives from a previously-established ABP equation of state [16, 89]. The homogeneous state with constant, spatially-uniform $\phi(\mathbf{x}) = \phi_0$, where $\mathbf{x}$ denotes position, becomes unstable to fluctuations in ϕ when the free energy is nonconvex ($\partial_\phi\tilde{\mu}_h < 0$). Therefore, the spinodal curve demarcating the limit of stability is given by $\partial_\phi\tilde{\mu}_h = 0$, shown by the black curves in Fig. 1; ϕ_0 represents the ABP volume fraction averaged over the entire system. Above this spinodal curve, the homogeneous state is linearly stable. Below the spinodal, ABPs spontaneously separate into dense and dilute phases, initially forming domains with a most unstable wavelength $\sim q_{\mathrm{sp}}^{-1} \equiv \sqrt{-2\kappa/\partial_\phi\tilde{\mu}_h}$ that coarsen over time via spinodal decomposition (Movie S1) as established previously [19, 89].

How do the features of MIPS change upon the introduction of chemotaxis ($\mathrm{Pe_C} > 0$)? Given a constant and uniform S, the homogeneous state is now described by spatially-uniform ABP and chemoattractant profiles, $\phi(\mathbf{x}) = \phi_0$ and $\tilde{c}(\mathbf{x}) = \tilde{c}_0$, where $\tilde{c}_0$ is given by the steady-state solution to Eq. (3), $\tilde{c}_0 = S/(k\phi_0)$. By perturbing this steady state with small-amplitude fluctuations $\delta\phi = \delta\hat{\phi}e^{i\mathbf{q}\cdot\mathbf{x}+\omega t}$ and $\delta\tilde{c} = \delta\hat{c}e^{i\mathbf{q}\cdot\mathbf{x}+\omega t}$ of spatial wavevector $\mathbf{q}$ and growth rate ω, we obtain the dispersion relation $\omega(q)$, given by Eq. (S33) of [60], where $q = |\mathbf{q}|$ is the wavenumber of a given mode. The homogeneous state is linearly stable if $\mathrm{Re}\ \omega < 0$, which is always true when $\partial_\phi\tilde{\mu}_h > 0$. We therefore focus our subsequent analysis on the spinodal region of non-chemotactic MIPS where $\partial_\phi\tilde{\mu}_h < 0$, and nondimensionalize $\mathbf{q}$ and ω by the characteristic non-chemotactic MIPS quantities q_{sp} and $\omega_{\mathrm{sp}} \equiv \omega(q_{\mathrm{sp}}; \mathrm{Pe_C} = 0)$.

As detailed in §3 of [60], the dispersion relation for chemotactic MIPS [Eq. (S37)] solely depends on three dimensionless parameters: $\alpha \equiv -M_0\phi_0\partial_\phi\tilde{\mu}_h/D_c$, which compares the collective ABP diffusivity $-M_0\phi_0\partial_\phi\tilde{\mu}_h$ to that of the chemoattractant; the Damköhler number $\mathrm{Da} \equiv k\phi_0/(2D_cq_{\mathrm{sp}}^2) = -\kappa k\phi_0/(D_c\partial_\phi\tilde{\mu}_h)$, which compares the rates of chemoattractant uptake and diffusion over the length scale $q_{\mathrm{sp}}^{-1}/\sqrt{2}$; and the reduced chemotactic Péclet number $\mathrm{Pe}'_{\mathrm{C}} \equiv \chi_0\tilde{c}_0/(-M_0\phi_0\partial_\phi\tilde{\mu}_h)$. Because the MIPS phase diagram is conventionally parameterized by ϕ_0 and $\mathrm{Pe_R}$, which together set $\partial_\phi\tilde{\mu}_h$ [Eq. (S5)], we also define versions of the three dimensionless parameters that are independent of these variables: $\alpha_0 \equiv M_0/D_c$, $\mathrm{Da}_0 \equiv \kappa k/D_c$, and $\mathrm{Pe_C}$ given earlier, such that $\alpha = -\alpha_0\phi_0\partial_\phi\tilde{\mu}_h$, $\mathrm{Da} = -\mathrm{Da}_0\phi_0/\partial_\phi\tilde{\mu}_h$, and $\mathrm{Pe}'_{\mathrm{C}} = -\mathrm{Pe_C}\cdot S/(k\phi_0^2\partial_\phi\tilde{\mu}_h)$. Furthermore, because the proportionality between $\mathrm{Pe}'_{\mathrm{C}}$ and $\mathrm{Pe_C}$ is scaled by S/k, without loss of generality, we fix the chemoattractant supply rate $S/k = 1$. Chemotactic MIPS is then parameterized by a total of five governing parameters: $\{\phi_0, \mathrm{Pe_R}, \alpha_0, \mathrm{Da}_0, \mathrm{Pe_C}\}$, as summarized in Table S1. Thus, to examine how chemotaxis influences MIPS, we first investigate how the conventional $\phi_0 - \mathrm{Pe_R}$ phase diagram of MIPS changes upon varying α_0, Da_0, and $\mathrm{Pe_C}$.

As detailed in §3 of [60] and summarized in Appendix A, our first main result from the linear stability analysis is that phase separation is suppressed by chemotaxis, but only when two criteria are *simultaneously* satisfied: (i) $\mathrm{Pe}'_{\mathrm{C}} \geq \mathrm{Pe}'_{\mathrm{C,crit}}$, and (ii) $\alpha \leq \alpha_{\mathrm{crit}}$, where $\mathrm{Pe}'_{\mathrm{C,crit}} = (1+\min\{\mathrm{Da}, 1\})^2/(4\cdot\min\{\mathrm{Da}, 1\})$ and $\alpha_{\mathrm{crit}} = 1 + 2\cdot\mathrm{Da} + 2\sqrt{\mathrm{Da}(1+\mathrm{Da})}$. We therefore designate the limits given by $\mathrm{Pe}'_{\mathrm{C}} = \mathrm{Pe}'_{\mathrm{C,crit}}$ and $\alpha = \alpha_{\mathrm{crit}}$ as "Boundary 1" and "Boundary 2"—shown in the $\mathrm{Pe_R} - \phi_0$ phase diagrams (Fig. 1) by the solid and red dotted curves, respectively. Boundary 1 is colored by the different values

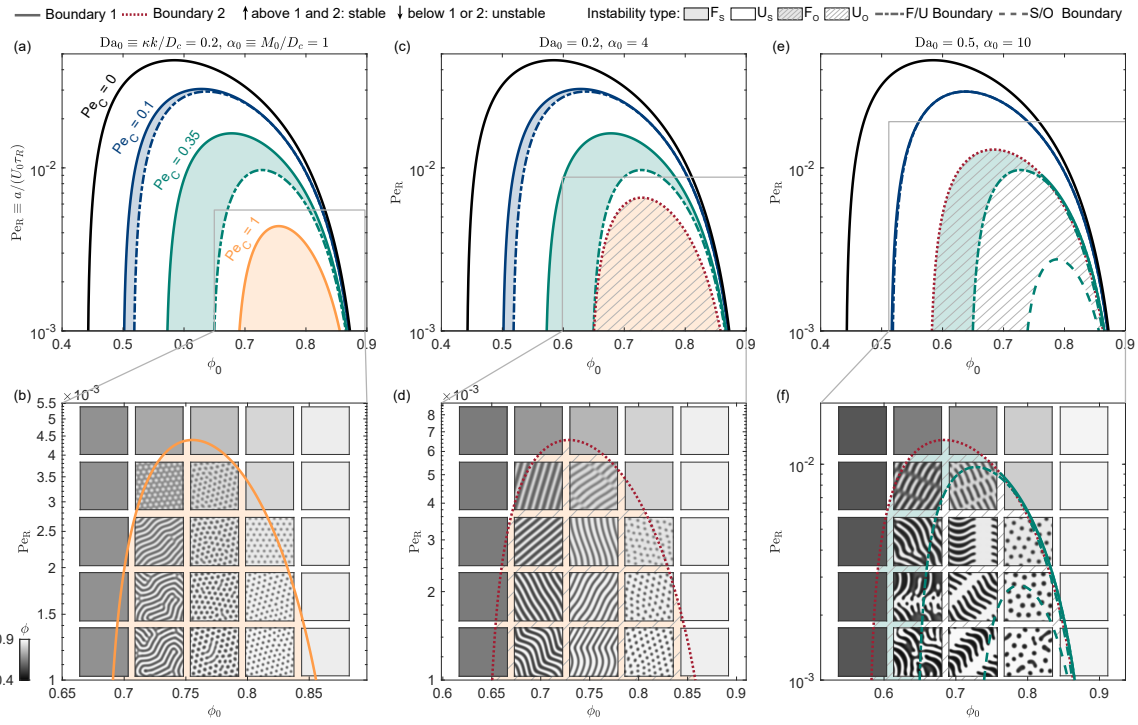

FIG. 1: Chemotaxis suppresses MIPS. (a, c, e) Phase diagram determined by linear stability analysis for different Da_0 and α_0; ϕ_0 represents the system-averaged ABP volume fraction. The black curve shows the limit of stability without chemotaxis, below which is conventional MIPS. The colored solid and red dotted curves show Boundaries 1 and 2, defined in the main text; different colors indicate different $\mathrm{Pe_C}$. Boundary 2 is below the horizontal axis in (a). The region above *both* Boundaries is stable (ABPs in the homogeneous state), while the region below *either* Boundary is unstable. The different instability types—finite (F) or unbounded (U), stationary (S) or oscillatory (O)—are denoted by the shaded, unshaded, non-hashed, and hashed regions, respectively. Dash-dotted and dashed curves indicate the boundaries between F/U and S/O instabilities, respectively. The predictions are corroborated by simulations (Movies S2-S4), snapshots of which are shown in (b, d, f), which focus on the grey boxed regions shown in (a, c, e). Snapshots in (b) and (d) correspond to $\mathrm{Pe_C} = 1$, while $\mathrm{Pe_C} = 0.35$ in (f).

of $\mathrm{Pe_C}$. Boundary 2 does not depend on $\mathrm{Pe_C}$. Criteria (i) and (ii) correspond to the regions above Boundaries 1 and 2, respectively; hence, the region above *both* Boundaries represents the stable regime in which the ABPs are in the homogeneous state, while conversely, the region below *either* Boundary 1 *or* 2 represents the unstable regime in which the ABPs phase separate.

As a starting example, we consider $\mathrm{Da}_0 = 0.2$ and $\alpha_0 = 1$, shown in Fig. 1(a). In this case, Boundary 2 is below the horizontal axis; hence, the system is linearly stable above Boundary 1 and unstable below it. Boundary 1 shifts to lower $\mathrm{Pe_R}$ and a narrower range of ϕ_0 with increasing $\mathrm{Pe_C}$. That is, the region of instability shrinks and phase separation is suppressed when chemotaxis is stronger. Numerical simulations at $\mathrm{Pe_C} = 1$ confirm this linear stability result: ABPs are in the homogeneous state above Boundary 1, but phase separate below it, as shown in Fig. 1(b). Intriguingly, the features of this phase separation appear to be fundamentally distinct from the spinodal decomposition observed in conventional non-chemotactic MIPS. For example, as shown in Movie S2, ABPs phase separate into finite-sized domains that remain stationary, and do not subsequently coarsen—unlike in conventional MIPS.

Next, upon increasing α_0 to 4, Boundary 1 remains unaltered, but Boundary 2 shifts upward, as shown in Fig. 1(c). As a result, for the case of $\mathrm{Pe_C} = 1$, Boundary 2 rises above Boundary 1, which is omitted since Boundary 2 now corresponds to the limit of stability, as confirmed by numerical simulations shown in Fig. 1(d). As shown in Movie S3, ABPs phase separate into finite-sized domains and bands that form traveling waves, a feature that is fundamentally distinct both from conventional MIPS and Fig. 1(b).

Finally, to highlight yet another distinct form of phase separation, we then increase both α_0 and Da_0 in Fig. 1(e), where Boundary 1 shifts downward while Boundary 2 shifts upward, part of which becomes the limit of stability for $\mathrm{Pe_C} = 0.35$, confirmed by simulations in Fig. 1(f). Strikingly, we find that throughout the unstable region,

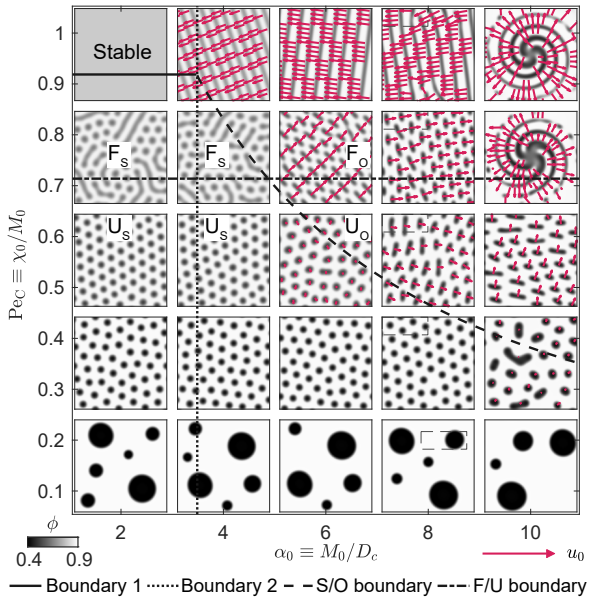

FIG. 2: Chemotaxis arrests phase separation and generates dynamic instabilities. Phase diagram is parameterized by α_0 and $\mathrm{Pe_C}$, holding $\phi_0 = 0.8$, $\mathrm{Pe_R} = 10^{-3}$, and $\mathrm{Da_0} = 0.5$ fixed. Different instability types predicted by our linear stability analysis are indicated using the same labels as in Fig. 1, again corroborated by simulations (Movie S7), snapshots of which are shown. Arrows show the local velocity field $\mathbf{u}$ relative to the characteristic velocity $u_0 \equiv M_0/\sqrt{\kappa} \sim U_0$; $|\mathbf{u}| < 0.005u_0$ vectors are omitted for clarity.

the patterns vary from traveling bands that are extended (shaded green + hashed region) or less extended (unshaded + hashed region) to domains that stretch, rotate, and translate (unshaded region below the green dashed curve), as shown in Movie S4.

Taken altogether, these results demonstrate that MIPS is suppressed when (1) the strength of chemotaxis, as quantified by $\mathrm{Pe_C}$, *and* (2) chemoattractant diffusivity relative to that of the ABPs, as quantified by α_0^{-1}, are sufficiently high. Moreover, our simulations reveal that the features of phase separation are dramatically altered by chemotaxis—with separated domains that initially can either be finite-sized or unbounded in space, and can either be stationary or exhibit complex oscillatory dynamics in time, depending on the values of $\{\phi_0, \mathrm{Pe_R}, \alpha_0, \mathrm{Da_0}, \mathrm{Pe_C}\}$. We summarize these results in the $\alpha_0 - \mathrm{Pe_C}$ phase diagram shown in Fig. 2, holding ϕ_0, $\mathrm{Pe_R}$, and $\mathrm{Da_0}$ fixed, and show the region of stability (which lies above Boundary 1 and to the left of Boundary 2 in the $\alpha_0 - \mathrm{Pe_C}$ plane shown) and snapshots of these different types of instability (animated in Movie S7) that we now seek to categorize.

Chemotaxis arrests phase separation. We first classify the instabilities by their distinct spatial characteristics. In particular, depending on the range of initially-unstable wavenumbers $q_- < q < q_+$ in the dispersion relation $\omega(q)$ [Eq. (S33)] derived using our linear stability analysis, we differentiate instabilities as being either finite-wavelength (F) when the unstable modes are spatially bounded ($q_- > 0$), and therefore phase-separated domains do not coarsen, or unbounded (U) when the unstable modes can instead extend indefinitely in space ($q_- = 0$) [90]. While conventional MIPS is a Type U instability [19, 43, 89], our second main result is that chemotaxis can give rise to Type F instabilities as well—as shown by the domains that do not coarsen in e.g., Movies S2–S3 noted earlier. Comparing the ABP (Movies S2–3) and chemoattractant (Movies S5–6) profiles reveals the underlying reason: ABPs in an extended, dense domain collectively establish a strong local chemoattractant gradient through uptake—which in turn causes them to bias their motion up the gradient and disperse away, arresting phase separation.

This behavior is also reflected in the simulations shown in Fig. 2 and Movie S7. For the example of $\alpha_0 = 2$ (left of Boundary 2), as $\mathrm{Pe_C}$ increases, the coarsening slows and eventually becomes arrested (§6 of [60]), forming finite-sized domains and stripes—ultimately reaching the homogeneous state at the largest $\mathrm{Pe_C}$ above Boundary 1. Examining the dispersion relations corroborates this observation (see Appendix B). Indeed, determining q_- directly from the dispersion relation yields the criterion that Type F is $\mathrm{Pe_C'} > 1$ (shaded regions in Fig. 1), while Type U is given by $\mathrm{Pe_C'} < 1$ (unshaded). The boundary between the two, given by $\mathrm{Pe_C'} = 1$ (Eq. (S68), is represented by the dash-dotted curves in Figs. 1 and 2. In all cases, our predictions agree well with the simulations, as detailed in §7 of [60]—thereby providing a description of how chemotaxis can arrest MIPS. Indeed, as described in §9 of [60], this description may help to rationalize previous observations of bacterial populations [7, 91].

Chemotaxis engenders complex oscillatory dynamics. We further classify the instabilities by their distinct temporal characteristics [43] — "Stationary" (S) if all unstable modes are non-oscillatory with $\mathrm{Im}\ \omega = 0$, or "Oscillatory" (O) if there exist unstable and oscillatory modes with $\mathrm{Re}\ \omega(q) > 0$ and $\mathrm{Im}\ \omega(q) \neq 0$. While conventional MIPS is a Type S instability, our third main result is that chemotaxis can give rise to Type O instabilities as well—e.g., Movies S3-4 noted earlier. This behavior is also reflected in Fig. 2 and Movie S7, and is again corroborated by examining the dispersion relations for the example of $\alpha_0 = 8$ (Appendix B). In this case, at large $\mathrm{Pe_C}$, chemotaxis proceeds more rapidly and the diffusing chemoattractant cannot equilibrate fast enough. As a result, variations in $\tilde{c}(\mathbf{x})$ lag behind $\phi(\mathbf{x})$ (Appendix B), driving sustained large-scale motion of the phase-separated domains [92, 93] e.g., through stretching, rotating, and translating, as indicated by the arrows in Fig. 2 showing the local velocity field $\mathbf{u}$.

The dispersion relation again yields a criterion for the Type O instability, shown as the hashed regions in Fig. 1. The Type S/O boundary [Eq. (S60)] is represented using the dashed curves in Figs. 1(e)-(f) and 2; in Fig. 1(c)-(d), this Boundary coincides with Boundary 2. We again observe good agreement between the predicted Type S/O boundary and the simulations [94]. Thus, our analysis provides a key first step toward explaining how the interplay between chemotaxis and chemoattractant diffusion can generate more complex phase separation dynamics than in conventional MIPS. Indeed, as described in §9 of [60], our results may help guide new experiments using synthetic materials [12, 95–101] to explore these rich physics. Our simulations also show other complex features, e.g., the quasi-ordered lattices in Fig. 2, whose description will require nonlinearities to be explicitly incorporated in the analysis; moreover, while here we examined a specific type of chemotaxis and MIPS, our theoretical framework can be readily extended to other forms of taxis and phase separation. We further describe these useful directions for future work in §10 of [60].

We acknowledge support from NSF Grants CBET-1941716, DMR-2011750, and EF-2124863, the Camille Dreyfus Teacher-Scholar Program, the Pew Biomedical Scholars Program, and a Princeton Bioengineering Initiative (PBI^2) Postdoctoral Fellowship.

APPENDIX A: LINEAR STABILITY ANALYSIS

Here, we provide a summary of the linear stability analysis in §3 of [60]. Substituting the small-amplitude perturbations $\delta\phi$ and $\delta\tilde{c}$ into linearized Eqs. 1, 2, and 3 yields

$$\omega\delta\hat{\phi} = -M_0\phi_0 q^2(\partial_\phi\tilde{\mu}_h + \kappa q^2)\delta\hat{\phi} + \chi_0\phi_0 q^2 f'(\tilde{c}_0)\delta\hat{c}, \quad (4)$$

$$\omega\delta\hat{c} = -D_c q^2\delta\hat{c} - k(g(\tilde{c}_0)\delta\hat{\phi} + \phi_0 g'(\tilde{c}_0)\delta\hat{c}). \quad (5)$$

§3E of [60] shows that the system is always linearly stable outside the spinodal region $\partial_\phi\tilde{\mu}_h > 0$. Therefore, we analyze the linear stability when $\partial_\phi\tilde{\mu}_h < 0$ below. Nondimensionalizing the wavenumber q and growth rate ω via $\tilde{q} = q/(\sqrt{2}q_{\rm sp})$ and $\tilde{\omega} = \omega/(4\omega_{\rm sp})$, we obtain the following quadratic equation for $\tilde{\omega}$,

$$\tilde{\omega}^2 + \left[\tilde{q}^4 - \left(1 - \frac{1}{\alpha}\right)\tilde{q}^2 + \frac{\mathrm{Da}}{\alpha}\right]\tilde{\omega} + \frac{\tilde{q}^2}{\alpha}\big((\tilde{q}^2-1)(\tilde{q}^2+\mathrm{Da}) + \mathrm{DaPe}'_{\rm C}\big) = 0. \quad (6)$$

The stability condition is that two solutions to the equation satisfy $\mathrm{Re}\ \tilde{\omega}_\pm(\tilde{q}) \le 0$ for all $\tilde{q}$, or equivalently $\tilde{\omega}_+\tilde{\omega}_- > 0$ and $\tilde{\omega}_+ + \tilde{\omega}_- < 0$.

Since

$$\tilde{\omega}_+\tilde{\omega}_- = \frac{\tilde{q}^2}{\alpha}\big((\tilde{q}^2-1)(\tilde{q}^2+\mathrm{Da}) + \mathrm{DaPe}'_{\rm C}\big), \quad (7)$$

when $\mathrm{Da} \le 1$, $\alpha\tilde{q}^{-2}\tilde{\omega}_+\tilde{\omega}_- \ge \mathrm{Da}(\mathrm{Pe}'_{\rm C} - 1)$. When $\mathrm{Da} > 1$, $\alpha\tilde{q}^{-2}\tilde{\omega}_+\tilde{\omega}_- \ge -\frac{(1+\mathrm{Da})^2}{4} + \mathrm{DaPe}'_{\rm C}$. Therefore, $\tilde{\omega}_+\tilde{\omega}_- > 0$ for all $\tilde{q}$ is equivalent to criterion (i) ($\mathrm{Pe}'_{\rm C} \ge \mathrm{Pe}'_{\rm C,crit}$).

Since

$$\tilde{\omega}_+ + \tilde{\omega}_- = -\tilde{q}^4 + \left(1 - \frac{1}{\alpha}\right)\tilde{q}^2 - \frac{\mathrm{Da}}{\alpha}, \quad (8)$$

when $\alpha \le 1$, $\tilde{\omega}_+ + \tilde{\omega}_- \le -\mathrm{Da}/\alpha < 0$. When $\alpha > 1$, $\tilde{\omega}_+ + \tilde{\omega}_- \le (1-\alpha^{-1})^2/4 - \mathrm{Da}/\alpha$. Therefore, $\tilde{\omega}_+ + \tilde{\omega}_- < 0$ for all $\tilde{q}$ is equivalent to criterion (ii) ($\alpha \le \alpha_{\rm crit}$).

In the main text, we define type U instability to be when the lower bound of the unstable wavenumber q_- is zero. As shown in §3C of [60], this condition is equivalent to requiring that the second order derivative of $\tilde{\omega}_+$ at $\tilde{q} = 0$ is positive, that is, $\tilde{\omega}''_+(\tilde{q}=0) = 2(1 - \mathrm{Pe}'_{\rm C}) > 0$, or $\mathrm{Pe}'_{\rm C} < 1$.

Oscillatory instability emerges when there exists $\tilde{q}$ for which $\mathrm{Re}\ \sigma(\tilde{q}) > 0$ and $\mathrm{Im}\ \sigma(\tilde{q}) \ne 0$, or equivalently $\tilde{\omega}_+\tilde{\omega}_- > 0$ and the determinant of Eq. 6 is negative. The first condition requires that criterion (ii) is not satisfied ($\alpha > \alpha_{\rm crit}$). For the second condition, because the determinant is

$$\Delta = \left[\tilde{q}^4 - \left(1 + \frac{1}{\alpha}\right)\tilde{q}^2 - \frac{\mathrm{Da}}{\alpha}\right]^2 - \frac{4\mathrm{DaPe}'_{\rm C}}{\alpha}\tilde{q}^2, \quad (9)$$

Δ becomes negative when $\mathrm{Pe}'_{\rm C}$ is sufficiently large. §3D of [60] derives the expression for the critical $\mathrm{Pe}'_{\rm C}$ above which both conditions are met.

APPENDIX B: THE ROLE OF CHEMOTAXIS IN ARRESTING PHASE SEPARATION AND GENERATING COMPLEX DYNAMICS.

As shown in Fig. 2 and Movie S7, for the example of $\alpha_0 = 2$ (left of Boundary 2), chemotaxis arrests phase separation with increasing $\mathrm{Pe}_{\rm C}$. Examining the dispersion relations in Fig. 3(a) corroborates this observation. At low non-zero $\mathrm{Pe}_{\rm C}$, the unstable modes extend to $q_- = 0$ (blue to green curves), indicating a Type U instability. By contrast, for the larger $\mathrm{Pe}_{\rm C} = 0.76$, $q_- > 0$ (chartreuse curve), indicating a Type F instability.

Also as shown in Fig. 2 and Movie S7, for the example of $\alpha_0 = 8$ (right of Boundary 2), chemotaxis arrests phase separation with increasing $\mathrm{Pe}_{\rm C}$. Examining the dispersion relations in Fig. 3(b) corroborates this observation. At low $\mathrm{Pe}_{\rm C}$ (blue and cyan curves), all unstable modes (with $\mathrm{Re}\ \omega > 0$) are stationary (having $\mathrm{Im}\ \omega = 0$), indicating a Type S instability; by contrast, at higher $\mathrm{Pe}_{\rm C}$ (green to orange curves), some unstable modes have $\mathrm{Im}\ \omega \ne 0$, indicating a Type O instability.

Comparing the ABP and chemoattractant profiles, $\phi(\mathbf{x})$ and $\tilde{c}(\mathbf{x})$ respectively, sheds light on the physics underlying these complex dynamics at large $\mathrm{Pe}_{\rm C}$ and α_0. Fig. 3(c) shows the illustrative case of $\alpha_0 = 8$ for the five different $\mathrm{Pe}_{\rm C}$ shown in (a). For the lowest two $\mathrm{Pe}_{\rm C}$, chemotaxis is weak, enabling $\tilde{c}(\mathbf{x})$ to equilibrate in response to changes in $\phi(\mathbf{x})$. Consequently, the phase-separated patterns remain stationary, reflective of a Type S instability. For larger $\mathrm{Pe}_{\rm C}$, however, chemotaxis proceeds more rapidly and the diffusing chemoattractant cannot equilibrate fast enough. As a result, variations in $\tilde{c}(\mathbf{x})$ lag behind $\phi(\mathbf{x})$, driving directed large-scale motion of the phase-separated domains [92, 93], reflective of a Type O instability.

* ssdatta@princeton.edu

[1] M. C. Marchetti, J. F. Joanny, S. Ramaswamy, T. B. Liverpool, J. Prost, M. Rao, and R. A. Simha, Hydrodynamics of soft active matter, Reviews of Modern Physics **85**, 1143 (2013).

[2] G. Gompper, R. G. Winkler, T. Speck, A. Solon, C. Nardini, F. Peruani, H. Löwen, R. Golestanian, U. B. Kaupp, L. Alvarez, T. Kiørboe, E. Lauga, W. C. K. Poon, A. DeSimone, S. Muiños-Landin, A. Fischer, N. A. Söker, F. Cichos, R. Kapral, P. Gaspard, M. Ripoll, F. Sagues, A. Doostmohammadi, J. M. Yeomans, I. S. Aranson, C. Bechinger, H. Stark, C. K. Hemelrijk, F. J. Nedelec, T. Sarkar, T. Aryaksama, M. Lacroix, G. Duclos, V. Yashunsky, P. Silberzan, M. Arroyo, and S. Kale, The 2020 motile active matter roadmap, Journal of Physics: Condensed Matter **32**, 193001 (2020).

[3] F. Mohajerani, X. Zhao, A. Somasundar, D. Velegol, and A. Sen, A theory of enzyme chemotaxis: From ex-

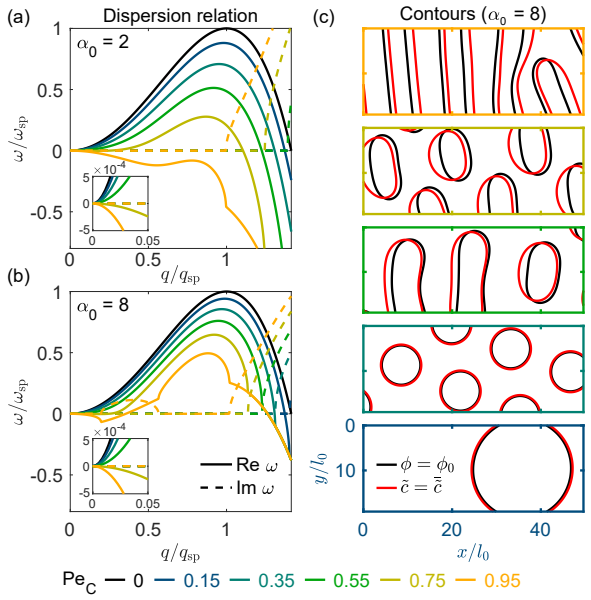

FIG. 3: (a-b) Dispersion relations $\omega(q)$ corresponding to $\alpha_0 = 2$ and $\alpha_0 = 8$ in Fig. 2; solid (dashed) lines show the Real (Imaginary) components. Insets show long wavelengths. (c) Magnified contours of $\phi = \phi_0$ and $\tilde{c} = \bar{\tilde{c}}$ (the spatial average of $\tilde{c}$) for the dashed rectangles in the snapshots of Fig. 2 at $\alpha_0 = 8$. Different colors in (a-c) show the different Pe$_C$ corresponding to the simulations shown in Fig. 2.

periments to modeling, Biochemistry **57**, 6256 (2018).

[4] J. Agudo-Canalejo, P. Illien, and R. Golestanian, Phoresis and enhanced diffusion compete in enzyme chemotaxis, Nano Letters **18**, 2711 (2018).

[5] A. Y. Jee, Y. K. Cho, S. Granick, and T. Tlusty, Catalytic enzymes are active matter, Proceedings of the National Academy of Sciences of the United States of America **115**, E10812 (2018).

[6] J. D. Murray, *Mathematical biology: I. An introduction* (Springer Science and Business Media., 2007).

[7] G. Liu, A. Patch, F. Bahar, D. Yllanes, R. D. Welch, M. C. Marchetti, S. Thutupalli, and J. W. Shaevitz, Self-driven phase transitions drive myxococcus xanthus fruiting body formation, Physical Review Letters **122**, 248102 (2019).

[8] R. Alert and X. Trepat, Physical models of collective cell migration, The Annual Review of Condensed Matter Physics is Annu. Rev. Condens. Matter Phys. 2020 **11**, 77 (2019).

[9] E. Scarpa and R. Mayor, Collective cell migration in development, Journal of Cell Biology **212**, 143 (2016).

[10] J. Palacci, S. Sacanna, A. P. Steinberg, D. J. Pine, and P. M. Chaikin, Living crystals of light-activated colloidal surfers, Science **339**, 936 (2013).

[11] I. Theurkauff, C. Cottin-Bizonne, J. Palacci, C. Ybert, and L. Bocquet, Dynamic clustering in active colloidal suspensions with chemical signaling, Physical Review Letters **108**, 268303 (2012).

[12] S. Palagi and P. Fischer, Bioinspired microrobots, Nature Reviews Materials **3**, 113 (2018).

[13] G. S. Redner, M. F. Hagan, and A. Baskaran, Structure and dynamics of a phase-separating active colloidal fluid, Physical Review Letters **110**, 055701 (2013).

[14] Y. Fily and M. C. Marchetti, Athermal phase separation of self-propelled particles with no alignment, Physical Review Letters **108**, 235702 (2012).

[15] M. E. Cates and J. Tailleur, Motility-induced phase separation, Annual Review of Condensed Matter Physics **6**, 219 (2015).

[16] S. C. Takatori and J. F. Brady, Towards a thermodynamics of active matter, Physical Review E **91**, 032117 (2015).

[17] M. E. Cates and J. Tailleur, When are active brownian particles and run-and-tumble particles equivalent? consequences for motility-induced phase separation, EPL (Europhysics Letters) **101**, 20010 (2013).

[18] J. Bialké, H. Löwen, and T. Speck, Microscopic theory for the phase separation of self-propelled repulsive disks, EPL **103**, 10.1209/0295-5075/103/30008 (2013).

[19] J. Stenhammar, A. Tiribocchi, R. J. Allen, D. Marenduzzo, and M. E. Cates, Continuum theory of phase separation kinetics for active brownian particles, Physical Review Letters **111**, 145702 (2013).

[20] E. Tjhung, C. Nardini, and M. E. Cates, Cluster phases and bubbly phase separation in active fluids: Reversal of the ostwald process, Physical Review X **8**, 031080 (2018).

[21] T. Speck, J. Bialke, A. M. Menzel, and H. Lowen, Effective cahn-hilliard equation for the phase separation of active brownian particles, Physical Review Letters **112**, 218304 (2014).

[22] M. E. Cates, D. Marenduzzo, I. Pagonabarraga, and J. Tailleur, Arrested phase separation in reproducing bacteria creates a generic route to pattern formation, Proceedings of the National Academy of Sciences of the United States of America **107**, 11715 (2010).

[23] H. C. Berg, Chemotaxis in bacteria :-:9050, Annual Review of Biophysics and bioengineering (1975).

[24] J. Cremer, T. Honda, Y. Tang, J. Wong-ng, M. Vergassola, and T. Hwa, Chemotaxis as a navigation strategy to boost range expansion, Nature **575**, 10.1038/s41586-019-1733-y (2019).

[25] X. Fu, S. Kato, J. Long, H. H. Mattingly, C. He, D. C. Vural, S. W. Zucker, and T. Emonet, Spatial self-organization resolves conflicts between individuality and collective migration, Nature Communications **9**, 10.1038/s41467-018-04539-4 (2018).

[26] T. Bhattacharjee, D. B. Amchin, J. A. Ott, F. Kratz, and S. S. Datta, Chemotactic migration of bacteria in porous media, Biophysj **120**, 3483 (2021).

[27] T. Bhattacharjee, D. B. Amchin, R. Alert, J. A. Ott, and S. S. Datta, Chemotactic smoothing of collective migration, eLife , 1 (2022).

[28] Y. Bai, C. He, P. Chu, J. Long, X. Li, and X. Fu, Spatial modulation of individual behaviors enables an ordered structure of diverse phenotypes during bacterial group migration, eLife **10**, 10.7554/eLife.67316 (2021).

[29] M. Seyrich, A. Palugniok, and H. Stark, Traveling concentration pulses of bacteria in a generalized keller-segel model, New Journal of Physics **21**, 10.1088/1367-2630/ab4522 (2019).

[30] S. Gude, E. Pinçe, K. M. Taute, A. B. Seinen, T. S. Shimizu, and S. J. Tans, Bacterial coexistence driven by motility and spatial competition, Nature **578**, 588

(2020).
[31] J. Saragosti, V. Calvez, N. Bournaveas, A. Buguin, P. Silberzan, and B. Perthame, Mathematical description of bacterial traveling pulses, PLoS Computational Biology **6**, 10.1371/journal.pcbi.1000890 (2010).
[32] J. A. Moore-Ott, S. Chiu, D. B. Amchin, T. Bhattacharjee, and S. S. Datta, A biophysical threshold for biofilm formation, eLife **11**, 10.7554/eLife.76380 (2022).
[33] H. Stark, Artificial chemotaxis of self-phoretic active colloids: Collective behavior, Accounts of Chemical Research **51**, 2681 (2018).
[34] O. Pohl and H. Stark, Dynamic clustering and chemotactic collapse of self-phoretic active particles, Physical Review Letters **112**, 238303 (2014).
[35] B. Liebchen and H. Löwen, Synthetic chemotaxis and collective behavior in active matter, Accounts of Chemical Research **51**, 2982 (2018).
[36] B. Liebchen, D. Marenduzzo, I. Pagonabarraga, and M. E. Cates, Clustering and pattern formation in chemorepulsive active colloids, Physical Review Letters **115**, 258301 (2015).
[37] B. Liebchen, D. Marenduzzo, and M. E. Cates, Phoretic interactions generically induce dynamic clusters and wave patterns in active colloids, Physical Review Letters **118**, 268001 (2017).
[38] B. Liebchen and D. Levis, Collective behavior of chiral active matter: Pattern formation and enhanced flocking, Physical Review Letters **119**, 058002 (2017).
[39] S. Saha, R. Golestanian, and S. Ramaswamy, Clusters, asters, and collective oscillations in chemotactic colloids, Physical Review E **89**, 062316 (2014).
[40] S. Saha, S. Ramaswamy, and R. Golestanian, Pairing, waltzing and scattering of chemotactic active colloids, New Journal of Physics **21**, 10.1088/1367-2630/ab20fd (2019).
[41] L. Varga, A. Libal, C. J. O. Reichhardt, and C. Reichhardt, Active regimes for particles on resource landscapes, Physical Review Research **4**, 013061 (2022).
[42] L. Varga, A. Libal, C. Reichhardt, and C. J. O. Reichhardt, Pattern formation and flocking for particles near the jamming transition on resource gradient substrates, Physical Review E **106**, 064602 (2022).
[43] M. C. Cross and P. C. Hohenberg, Pattern formation outside of equilibrium, Reviews of Modern Physics **65**, 851 (1993).
[44] S. Kondo and T. Miura, Reaction-diffusion model as a framework for understanding biological pattern formation, Science **329**, 1616 (2010).
[45] M. Bär, R. Großmann, S. Heidenreich, and F. Peruani, Self-propelled rods: Insights and perspectives for active matter, Annual Review of Condensed Matter Physics **11**, 441 (2020).
[46] D. Zwicker, A. A. Hyman, and F. Julicher, Suppression of ostwald ripening in active emulsions, Physical Review E **92**, 012317 (2015).
[47] D. Zwicker, R. Seyboldt, C. A. Weber, A. A. Hyman, and F. Jülicher, Growth and division of active droplets provides a model for protocells, Nature Physics **13**, 408 (2017).
[48] A. M. Menzel and H. Lowen, Traveling and resting crystals in active systems, Physical Review Letters **110**, 055702 (2013).
[49] A. Ziepke, I. Maryshev, I. S. Aranson, and E. Frey, Multi-scale organization in communicating active matter, Nature Communications **13**, 6727 (2022).
[50] S. Saha, J. Agudo-Canalejo, and R. Golestanian, Scalar active mixtures: The nonreciprocal cahn-hilliard model, Physical Review X **10**, 041009 (2020).
[51] Z. You, A. Baskaran, and M. C. Marchetti, Nonreciprocity as a generic route to traveling states, Proceedings of the National Academy of Sciences **117**, 19767 (2020).
[52] J. van der Kolk, F. Rasshofer, R. Swiderski, A. Haldar, A. Basu, and E. Frey, Anomalous collective dynamics of auto-chemotactic populations (2022).
[53] R. Matas-Navarro, R. Golestanian, T. B. Liverpool, and S. M. Fielding, Hydrodynamic suppression of phase separation in active suspensions, Physical Review E **90**, 032304 (2014).
[54] R. M. Navarro and S. M. Fielding, Clustering and phase behaviour of attractive active particles with hydrodynamics, Soft Matter **11**, 7525 (2015).
[55] S. Yin and L. Mahadevan, Contractility-induced phase separation in active solids, (2022).
[56] M. Z. Bazant, Thermodynamic stability of driven open systems and control of phase separation by electroautocatalysis, Faraday Discussions **199**, 423 (2017).
[57] R. Adkins, I. Kolvin, Z. You, S. Witthaus, M. C. Marchetti, and Z. Dogic, Dynamics of active liquid interfaces, Science **377**, 768 (2022).
[58] A. M. Tayar, F. Caballero, T. Anderberg, O. A. Saleh, M. C. Marchetti, and Z. Dogic, Controlling liquid-liquid phase behavior with an active fluid (2022).
[59] F. Caballero and M. C. Marchetti, Activity-suppressed phase separation, Physical Review Letters **129**, 268002 (2022).
[60] See the supplemental material at [url], which includes Refs. [61–76].
[61] J. Tailleur and M. E. Cates, Statistical mechanics of interacting run-and-tumble bacteria, Physical Review Letters **100**, 218103 (2008).
[62] L. Shampine and M. Reichelt, Ode matlab solvers, Journal of Scientific Computing **18**, 1 (1997).
[63] H. Furukawa, Spinodal decomposition of two-dimensional fluid mixtures: A spectral analysis of droplet growth, Physical Review E - Statistical Physics, Plasmas, Fluids, and Related Interdisciplinary Topics **61**, 1423 (2000).
[64] M. Laradji, S. Toxvaerd, and O. G. Mouritsen, Molecular dynamics simulation of spinodal decomposition in three-dimensional binary fluids, Physical Review Letters **77**, 2253 (1996).
[65] S. Mao, D. Kuldinow, M. P. Haataja, and A. Košmrlj, Phase behavior and morphology of multicomponent liquid mixtures, Soft Matter **15**, 1297 (2019).
[66] A. J. Bray, Theory of phase-ordering kinetics, Advances in Physics **51**, 481 (2002).
[67] M. E. Cates, Diffusive transport without detailed balance in motile bacteria: Does microbiology need statistical physics?, Reports on Progress in Physics **75**, 10.1088/0034-4885/75/4/042601 (2012).
[68] I. Buttinoni, G. Volpe, F. Kummel, G. Volpe, and C. Bechinger, Active brownian motion tunable by light, Journal of Physics Condensed Matter **24**, 10.1088/0953-8984/24/28/284129 (2012).
[69] J. Stenhammar, R. Wittkowski, D. Marenduzzo, and M. E. Cates, Light-induced self-assembly of active rectification devices, Science Advances **2**, 1 (2016).
[70] J. Arlt, V. A. Martinez, A. Dawson, T. Pilizota, and

W. C. Poon, Painting with light-powered bacteria, Nature Communications **9**, 1 (2018).
[71] G. Frangipane, D. Dell'Arciprete, S. Petracchini, C. Maggi, F. Saglimbeni, S. Bianchi, G. Vizsnyiczai, M. L. Bernardini, and R. di Leonardo, Dynamic density shaping of photokinetic e. coli, eLife **7**, 1 (2018).
[72] E. F. Keller and L. A. Segel, Initiation of slime mold aggregation viewed as an instability, Journal of Theoretical Biology **26**, 399 (1970).
[73] E. Sesé-Sansa, I. Pagonabarraga, and D. Levis, Velocity alignment promotes motility-induced phase separation, EPL **124**, 10.1209/0295-5075/124/30004 (2018).
[74] M. N. V. D. Linden, L. C. Alexander, D. G. Aarts, and O. Dauchot, Interrupted motility induced phase separation in aligning active colloids, Physical Review Letters **123**, 10.1103/PhysRevLett.123.098001 (2019).
[75] A. Wysocki, R. G. Winkler, and G. Gompper, Propagating interfaces in mixtures of active and passive brownian particles, New Journal of Physics **18**, 123030 (2016).
[76] J. Zhang, R. Alert, J. Yan, N. S. Wingreen, and S. Granick, Active phase separation by turning towards regions of higher density, Nature Physics **17**, 961 (2021).
[77] R. Alert, A. Martínez-Calvo, and S. S. Datta, Cellular sensing governs the stability of chemotactic fronts, Physical Review Letters **128**, 148101 (2022).
[78] H. Masoud and M. J. Shelley, Collective surfing of chemically active particles, Physical Review Letters **112**, 10.1103/PhysRevLett.112.128304 (2013).
[79] B. Liebchen and A. K. Mukhopadhyay, Interactions in active colloids, Journal of Physics: Condensed Matter **34**, 083002 (2022).
[80] M. P. Brenner, L. S. Levitov, and E. O. Budrene, Physical mechanisms for chemotactic pattern formation by bacteria, Biophysical Journal **74**, 1677 (1998).
[81] M. A. Herrero and J. J. L. Velázquez, Chemotactic collapse for the keller-segel model, Journal of Mathematical Biology **35**, 177 (1996).
[82] E. F. Keller and L. A. Segel, Model for chemotaxis, Journal of Theoretical Biology **30**, 225 (1971).
[83] E. F. Keller and L. A. Segel, Traveling bands of chemotactic bacteria: A theoretical analysis, Journal of Theoretical Biology **30**, 235 (1971).
[84] J. D. Murray, *Mathematical Biology II: Spatial Models and Biomedical Applications*, edited by J. D. Murray, Vol. 18 (Springer New York, 2003).
[85] R. Colin, B. Ni, L. Laganenka, and V. Sourjik, Multiple functions of flagellar motility and chemotaxis in bacterial physiology (2021).
[86] J. Adler, Chemotaxis in bacteria, Science **153**, 708 (1966).
[87] P. H. Colberg and R. Kapral, Many-body dynamics of chemically propelled nanomotors, Journal of Chemical Physics **147**, 10.1063/1.4997572 (2017).
[88] S. Mahdisoltani, R. B. A. Zinati, C. Duclut, A. Gambassi, and R. Golestanian, Nonequilibrium polarity-induced chemotaxis: Emergent galilean symmetry and exact scaling exponents, Physical Review Research **3**, 10.1103/PhysRevResearch.3.013100 (2021).
[89] S. Takatori, W. Yan, and J. Brady, Swim pressure: Stress generation in active matter, Physical Review Letters **113**, 028103 (2014).
[90] V. M. Worlitzer, G. Ariel, A. Be'er, H. Stark, M. Bär, and S. Heidenreich, Motility-induced clustering and meso-scale turbulence in active polar fluids, New Journal of Physics **23**, 033012 (2021).
[91] E. O. Budrene and H. C. Berg, Complex patterns formed by motile cells of escherichia coli, Nature **349**, 630 (1991).
[92] S. Michelin, E. Lauga, and D. Bartolo, Spontaneous autophoretic motion of isotropic particles, Physics of Fluids **25**, 061701 (2013).
[93] S. Michelin and E. Lauga, Phoretic self-propulsion at finite péclet numbers, Journal of Fluid Mechanics **747**, 572 (2014).
[94] We note, however, that below the S/O boundary shown by the dashed curve in Fig. 1(e)–(f), the simulations still show some initial non-stationary behavior—reflecting the limitation of our linear stability analysis, which is strictly only applicable to conditions close to the initial homogeneous state.
[95] P. Roca-Cusachs, R. Sunyer, and X. Trepat, Mechanical guidance of cell migration: lessons from chemotaxis, Current Opinion in Cell Biology **25**, 543 (2013).
[96] A. Shellard and R. Mayor, All roads lead to directional cell migration, Trends in Cell Biology **30**, 852 (2020).
[97] S. SenGupta, C. A. Parent, and J. E. Bear, The principles of directed cell migration, Nature Reviews Molecular Cell Biology **22**, 529 (2021).
[98] R. Sunyer, V. Conte, J. Escribano, A. Elosegui-Artola, A. Labernadie, L. Valon, D. Navajas, J. M. García-Aznar, J. J. Muñoz, P. Roca-Cusachs, and X. Trepat, Collective cell durotaxis emerges from long-range intercellular force transmission, Science **353**, 1157 (2016).
[99] R. Alert and J. Casademunt, Role of substrate stiffness in tissue spreading: Wetting transition and tissue durotaxis, Langmuir **35**, 7571 (2019).
[100] D. J. Cohen, W. J. Nelson, and M. M. Maharbiz, Galvanotactic control of collective cell migration in epithelial monolayers, Nature Materials **13**, 409 (2014).
[101] M. Mijalkov, A. McDaniel, J. Wehr, and G. Volpe, Engineering sensorial delay to control phototaxis and emergent collective behaviors, Physical Review X **6**, 011008 (2016).